PHYSICAL REVIEW B **88**, 214104 (2013)

Charge ordering transition in $GdBaCo_2O_5$: Evidence of reentrant behavior

M. Allieta,[1,*] M. Scavini,[1,2] L. Lo Presti,[1,2,3] M. Coduri,[1] L. Loconte,[1] S. Cappelli,[1] C. Oliva,[1] P. Ghigna,[4]
P. Pattison,[5,6] and V. Scagnoli[7,8]
[1]*Dipartimento di Chimica, Università degli Studi di Milano, Via Camillo Golgi 19, I-20133 Milano, Italy*
[2]*CNR-ISTM, and INSTM Unit Milan, Via Camillo Golgi 19, I-20133 Milan, Italy*
[3]*Centre for Materials Crystallography, Århus University, Langelandsgade 140, DK-8000 Århus C, Denmark*
[4]*Dipartimento di Chimica, Università degli Studi di Pavia, Viale Taramelli 16, 27100 Pavia, Italy*
[5]*Swiss-Norwegian Beamlines, European Synchrotron Radiation Facility, 6 rue Jules Horowitz, BP 220, 38043 Grenoble Cedex 9, France*
[6]*Laboratory of Crystallography, BSP, Ecole polytechnique fédérale de Lausanne, CH-1015 Lausanne, Switzerland*
[7]*European Synchrotron Radiation Facility, 6 rue Jules Horowitz, BP 220, 38043 Grenoble Cedex 9, France*
[8]*Paul Scherrer Institut, CH-5232 Villigen PSI, Switzerland*
(Received 21 July 2013; published 4 December 2013)

We present a detailed study on the charge ordering transition in a $GdBaCo_2O_{5.0}$ system by combining high-resolution synchrotron powder/single-crystal diffraction with electron paramagnetic resonance experiments as a function of temperature. We found a second-order structural phase transition at $T_{CO} = 247$ K (*Pmmm* to *Pmma*) associated with the onset of long-range charge ordering. At $T_{min} \approx 1.2T_{CO,}$ the electron paramagnetic resonance linewidth rapidly broadens, providing evidence of antiferromagnetic spin fluctuations. This likely indicates that, analogously to manganites, the long-range antiferromagnetic order in $GdBaCo_2O_{5.0}$ sets in at $\approx T_{CO}$. Pair distribution function analysis of diffraction data revealed signatures of structural inhomogeneities at low temperature. By comparing the average and local bond valences, we found that above T_{CO} the local structure is consistent with a fully random occupation of Co^{2+} and Co^{3+} in a 1:1 ratio and with a complete charge ordering below T_{CO}. Below $T \approx 100$ K the charge localization is partially melted at the local scale, suggesting a reentrant behavior of charge ordering. This result is supported by the weakening of superstructure reflections and the temperature evolution of electron paramagnetic resonance linewidth that is consistent with paramagnetic reentrant behavior reported in the $GdBaCo_2O_{5.5}$ parent compound.

DOI: 10.1103/PhysRevB.88.214104 PACS number(s): 75.47.−m, 64.70.K−, 61.05.cp, 76.30.−v

I. INTRODUCTION

Charge ordering (CO) observed in mixed valence perovskites is an intriguing phenomenon which has attracted a lot of interest in the past two decades.[1–6] The stabilization of CO depends on the commensurability of the charge carrier density with respect to the lattice periodicity and is driven by the competition of the intersite Coulomb and kinetic energies of electrons. The onset of CO phase triggered, e.g., by temperature (T) gives rise to an abrupt change in the transport and/or magnetic properties, reflecting an intricate interplay between charge, spin, orbital, and lattice degrees of freedom.[1–6]

One of the most remarkable examples of perovskitic oxides showing CO is the colossal magnetoresistive (CMR) $R_{0.5}A_{0.5}MnO_3$ (R, trivalent ion; A, Ca, Sr) manganites.[1,3] In these systems the charge carriers localization due to the occurrence of a Mn^{3+}/Mn^{4+} CO pattern is accompanied by a sudden increase of the electrical resistivity and by the onset of antiferromagnetic (AFM) phase at $T_N \leqslant T_{CO}$.[1,3]

Similar effects have been observed for the layered perovskite like compounds $LnBaCo_2O_{5+\delta}$ (Ln, lanthanide or Y).[5–7] These systems display a larger CMR effect than Mn-based perovskites and a variety of magnetic and transport properties, depending on oxygen concentration δ.[7] In particular, δ affects the mixed valence state of the cobalt ions, resulting in different Co^{2+}/Co^{3+} and Co^{4+}/Co^{3+} ratios with cobalt species stabilizing in several spin states.[5–9] In the case of the $LnBaCo_2O_{5.0}$ system ($Ln = Y$,[5] Tb,[6] Dy,[6] Ho[6]), where the Co^{2+}/Co^{3+} ratio equals 1, neutron powder diffraction (NPD) shows the insurgence of both charge and magnetic ordering associated with structural phase transitions. In the high-T paramagnetic (PM) state, these compounds display a tetragonal structure $P4/mmm$ and an $a \times a \times 2a$ cell metric, where a is the primitive cubic perovskite lattice parameter [Fig. 1(a)].[5,6,8] At $T \approx 350$ K, these systems undergo a structural phase transition to an orthorhombic-distorted lattice with *Pmmm* and an $a \times a \times 2a$ cell metric [Fig. 1(b)]. Despite the symmetry lowering, a unique Co site in a square pyramidal environment is still present in this phase.[5,6,8] The temperature dependence of magnetization of $YBaCo_2O_5$ — the only known $LnBaCo_2O_5$ compound with nonmagnetic Ln ions — suggested the occurrence of magnetic order associated with the structural phase transition around $T = 350$ K.[5–7] However, a more marked anomaly at $T \approx 220$ K is evident in the magnetization profile, which leads the assignment of the more intricate magnetic transition.

Below $T \approx 210$ K, the NPD measurements suggested the occurrence of another structural phase transition leading to a change of both cell metric and crystal symmetry. In this new low-T phase with *Pmma* and an $a \times 2a \times 2a$ cell metric[5,6] [Fig. 1(c)], two distinct Co sites are present and the transition can be interpreted in terms of CO.[5,6] The AFM structure in the charge ordered state is qualitatively explained by Goodenough-Kanamori (GK) rules for superexchange. The $\approx 1\mu_B$ difference between the refined magnetic moments of the nonequivalent Co sites at saturation is fully consistent with a complete Co^{2+}/Co^{3+} separation.[6] However, the bond valence sums (BVSs) calculated for the Co-O distances are far from the ideal $+2$ and $+3$ values, suggesting that

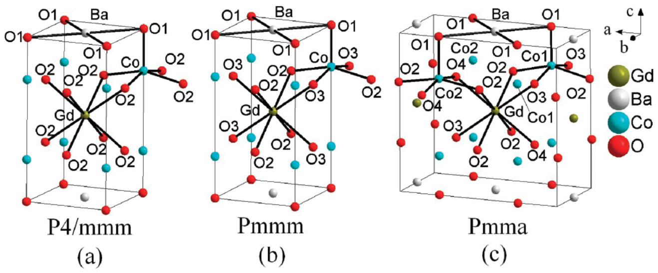

FIG. 1. (Color online) Packing and atom numbering schemes for each of the three phases of $GdBaCo_2O_5$: *P*4/*mmm* (a), *Pmmm* (b), and *Pmma* (c). For each symmetry-independent metal ion, its next-neighbor oxygen coordination environment is highlighted by black bonds.

only partial charge redistribution arises at T_{CO}. In addition, the occurrence of magnetic ordering at higher temperature than for long-range CO is opposite of what is observed in Mn-based compounds. This is the signature of a more complex scenario,[5,6,8] indicating that magnetic, electronic, and structural properties of $Ln\mathrm{BaCo_2O_{5.0}}$ systems still remain to be reconciled in a self-consistent picture.

In $GdBaCo_2O_{5.0}$ (GBCO), the occurrence of a CO transition below $T \approx 250$ K has been suggested by heat capacity[10] and internal friction[11] measurements. However, the existence of a CO-driven structural phase transition in this compound still remains unproven to date.[10,11] In a previous work,[8] we assigned the correct space group of GBCO at room temperature and we carefully studied the *P*4/*mmm* to *Pmmm* phase transition across $T \approx 350$ K. Here, we focus on the CO transition by combining x-ray powder diffraction (XRPD), synchrotron single-crystal x-ray diffraction (SCD), and EPR spectroscopy on GBCO. These techniques are sensitive either to CO or to the magnetic degree of freedom, allowing us to explore the transition from both the structural and the relaxation points of view.

As a result, we deduced the presence of a second-order structural phase transition associated with CO at $T = 247$ K. By cooling down to $T \approx 100$ K, we observed a local structural response consistent with a reentrant behavior of CO by using the pair distribution function (PDF) technique. The electron paramagnetic resonance (EPR) measurements suggest that the origin of CO as well as reentrant behavior is driven by an intimate interplay of electron localization and magnetic spin (dis)ordering.

II. EXPERIMENT

The same single-crystal and powdered GBCO samples employed in our previous study[8] were used for the present diffraction measurements with synchrotron radiation. SCD experiments were performed at the BM1A station of the Swiss-Norwegian beamline of the European Synchrotron Radiation Facility (ESRF, Grenoble, France). Data were recorded by double-crystal Si(111) monochromated x-ray radiation [$\lambda = 0.70826(2)$ Å] on a Kuma KM6-CH six-circle κ goniometer equipped with an Oxford diffraction CCD area detector and an Oxford Cryosystems N_2 gas blower. The sample was mounted on the top of a glass capillary fiber and SCD data collections were performed at nine different temperatures between 100 K and 380 K by three ω scans (132°, 136°, and 216° wide) with $\Delta\omega = 1°$ steps at fixed 2ϑ, κ, and φ axes (respectively 30°, 30°, 0°; 30°, $-45°$, 0°; 0°, 0°, 180°). Overall, this scheme provided, on average, an ≈97% complete dataset within the Cu-sphere resolution ($\sin\vartheta/\lambda = 0.652$ Å^{-1}). Moreover, the temperature evolution of the intensity of the *Pmma* (116) reflection, extinct in the high-T phases, was monitored by repeated φ scans.

CRYSALYSPRO[12] was employed to perform the data collection and reduction procedures. The unit cell parameters at each temperature (see Table S1 in the Supplemental Material[13]) were determined from least-squares fitting of the orientation matrix against the observed peak positions of, on average, ≈800 intense reflections. Empirical absorption correction based on multiple measures of equivalent reflections was applied to all the data sets according to the SCALE3 ABSPACK algorithm.[12] The crystal structure at each temperature was refined with SHELX.[14] Assessment of the sample quality can be found in the Supplemental Material.[13]

XRPD experiments were performed at the ID31 beamline of the ESRF by selecting $\lambda = 0.39620(5)$ Å. Twelve patterns in the $0° \leqslant 2\vartheta \leqslant 50°$ range data were collected for 1 h counting time between 5 K and 298 K. The sample was cooled down to 80 K by using a N_2 gas blower (Oxford Cryosystems), whereas a liquid-helium-cooled cryostat was employed to achieve the lowest temperature. Moreover, some patterns were collected at $\lambda = 0.35422(5)$ Å in the $80\ \mathrm{K} \leqslant T \leqslant 400$ K range. In particular, at selected temperatures ($T = 80$, $T = 180$ K, and $T = 298$ K) several scans were summed up for 7 h counting time ($Q_{\max} \approx 27$ Å^{-1}) to achieve statistical significance for PDF analysis.

Data were analyzed using the Rietveld method as implemented in the GSAS software suite.[15] Absorption correction was performed through the Lobanov empirical formula implemented for the Debye-Scherrer geometry. Line profiles were fitted using a modified pseudo-Voigt function accounting for asymmetry correction. In the last refinement cycles, scale factor(s), cell parameters, positional coordinates, and isotropic thermal parameters were allowed to vary as well as background and line profile parameters.

EPR measurements were performed at a Bruker ELEXSYS spectrometer equipped with an ER4102ST standard rectangular cavity at X band (9.4 GHz) frequency every 5 K in the temperature range 115 K–450 K. A powdered sample was placed into a quartz tube and the derivative dP/dH of power P absorbed was recorded as a function of the static magnetic field H.

III. RESULTS

A. SCD and XRPD across the CO transition

To probe the occurrence of low T structural phase transitions associated with possible CO effects, the reciprocal lattice as determined from SCD data was carefully screened to detect possible superstructure reflections. Actually, some commensurate superstructure diffraction spots with $h/2$ indices clearly appeared below 250 K, implying the low-temperature doubling of the cell axis. Conversely, no recognizable superstructure peaks were detected above $T \approx 250$ K.

SCD structural models as a function of T were obtained within the spherical atom approximation,[16] with the thermal

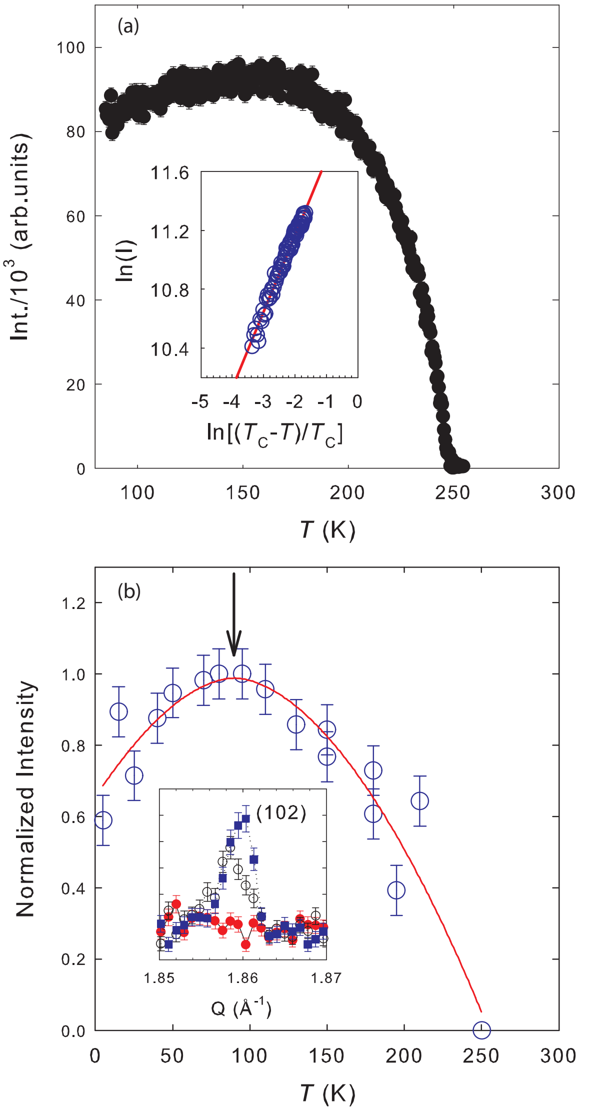

FIG. 2. (Color online) (a) Temperature dependence of intensity of the *Pmma* (116) superstructure reflection (circles). (Inset) ln-ln plot of the intensity versus $(T_c - T)/T_c$. (b) The temperature evolution of *Pmma* (102) reflection as collected at ID31 is reported as an example (open circles). The arrow indicates the onset of the intensity weakening. The inset shows XRPD profiles related to (102) reflection across the CO transition. Note that the intensity of superstructure reflections is much higher than the error bars given by the background.

motion of heavy-metal atoms modeled as anisotropic. The *Pmmm* room-temperature structure was employed as a suitable starting point for refining the positional and thermal motion parameters down to 250 K. Below $T = 250$ K, we adopted the structural *Pmma* model by Fauth *et al.*[6] as a starting point for the least-squares refinement procedure.[6] Table S1 of the Supplemental Material[13] summarizes the final statistics of the structural refinements, together with relevant details of the SCD experiments.

As reported in a similar structural study,[17] the transition from *Pmmm* to *Pmma* with an $a \times 2a \times 2a$ unit cell can be followed by the temperature dependence of (hkl) reflections with $h = 2n + 1$ and $l \neq 0$. Figure. 2(a) shows the temperature dependence of the intensity of the *Pmma* (116) superstructure reflection, which is extinct in the *Pmmm* phase. On the basis of these results, $T_{CO} = 247$ K can be assumed as a reasonable estimate for the CO transition temperature, as at this temperature the (116) superstructure reflection begins to be clearly significant (≈2 estimated standard deviation's) with respect to the background. According to the critical equation $I(T) = I(0)(T_c - T/T_c)^{\beta}$ with $T_c = T_{CO} = 247$ K, the least-squares estimate of the critical exponent β came out as large as 0.483(5) [inset of Fig. 2(a)], quite close to the ideal value for a second-order transition ($\beta = 0.5$). It is worth noting that, for $T < \approx 120$ K, the temperature dependence of (116) shows a slightly positive slope.

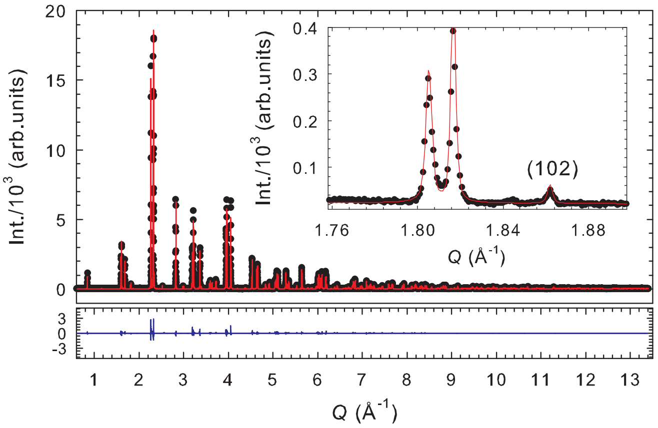

FIG. 3. (Color online) Measured (dots) and calculated (line) powder diffraction patterns and residuals (bottom line) for GBCO at $T = 5$ K and at $\lambda = 0.39620(5)$ Å. The inset shows a magnified view of the low-angle diffraction peaks where the CO superlattice reflection is clearly shown.

Clear signature of the CO transition was also found by analyzing the XRPD patterns through, e.g., the appearance of the *Pmma* (102) reflection across T_{CO} [Fig. 2(b), inset]. An accurate investigation of XRPD patterns does not reveal further peaks splitting as well as superstructure reflections corresponding to a modulation of an $a \times 2a \times 2a$ periodicity down to 5 K.

The structural parameters obtained from SCD data were used as starting values to perform Rietveld refinements against XRPD data as a function of temperature. Figure 3 shows an example of the Rietveld refinement performed at 5 K. From the quality of the fit it can be seen that XRPD patterns in the CO state can be well reproduced down to the lowest temperature by the *Pmma* superstructure. In Table S2 of the Supplemental Material,[13] selected structural data and agreement factors obtained for all patterns collected at different temperatures are listed. In *Pmmm* and *Pmma* structural models, we constrained isotropic thermal parameters related to oxygen positions to be the same.

In Fig. 4, we present the refined lattice parameters and cell volume as a function of T obtained by SCD and XRPD. A reduced orthorhombic cell metric was used for comparison purposes between the *Pmmm* and *Pmma* structures. As previously reported, the structure is tetragonal at $T > 350$ K and with decreasing T the orthorhombic distortion turns out to be appreciable in terms of the lattice metrics.[8] In particular, below $T = 350$ K the distortion becomes more evident and

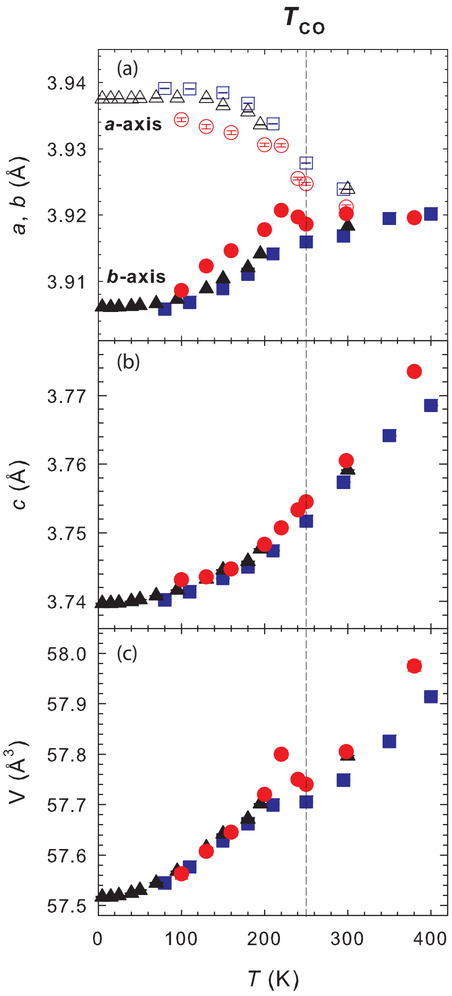

FIG. 4. (Color online) Temperature dependence of the (a) *a* and *b* axes, (b) *c* axis, and (c) unit cell volume. Solid and open circles are data from SCD; solid and open squares and triangles are data from XRPD.

the difference between *a* and *b* cell edges increases toward the CO transition (see Fig. 4). The *a* axis suddenly increases while the *b* axis steeply decreases at $T < T_{CO}$ and this anisotropic thermal expansion of the unit cell parameters is maintained down to $T \approx 100$ K. Below this temperature, both the axes reach a plateau by approaching constant values down to $T = 5$ K. This complex behavior suggests an intricate interplay between CO and the atomic interactions on the *ab* plane of GBCO.

It is worth noting that, as shown in Figs. 4(a) and 4(c), there are some differences between the results obtained from the SCD and XRPD techniques. By approaching the T_{CO} from above, *a* and *b* axes obtained from the two techniques are in fairly good agreement up to 298 K, but for $T < T_{CO}$ the anisotropic thermal expansion of the unit cell parameters seems to be different. In particular, in SCD results also the *b* lattice parameter exhibits a small lengthening across transition, resulting in an overall increase of the unit cell volume at T_{CO} [Fig. 4(c), solid circles]. This behavior was not detected by XRPD that, on the contrary, found only a weak variation of the slope of the temperature dependence of *V* across T_{CO}. However, looking at the general trends of the structural parameters across the CO transition (Fig. 4), we can say that—at least qualitatively—SCD and XRPD gave similar results. In the following discussion, we focus on the Co valence states and their interplay with the corresponding average Co coordination geometries.

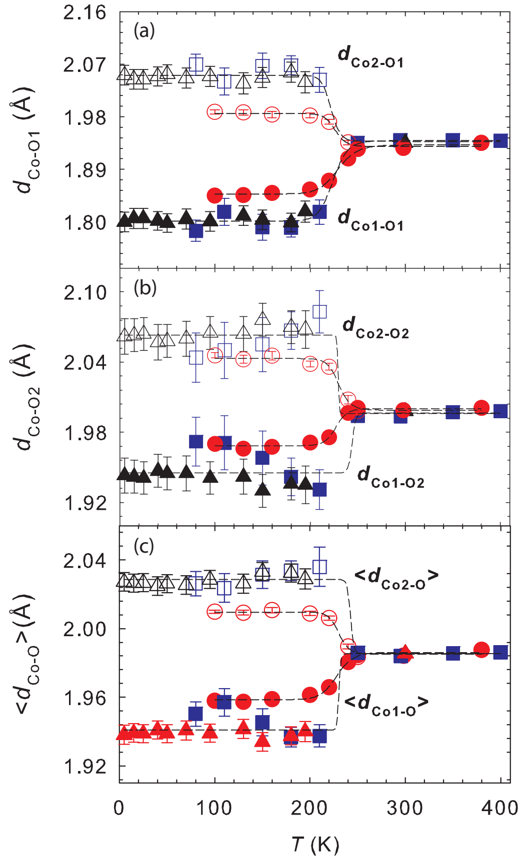

FIG. 5. (Color online) Temperature dependence of (a), (b) selected Co-O and (c) average ⟨Co-O⟩ distances. Solid and open circles are data from SCD; solid and open squares and triangles are data from XRPD. Dashed lines are guides for the eye.

Selected Co-O distances ($d_{Co\text{-}O}$) as a function of *T* are reported in Figs. 5(a) and 5(b). The presence of two distinct Co crystallographic sites in the *Pmma* CO phase gives rise to an anisotropic thermal expansion of $d_{Co\text{-}O}$. In particular, by decreasing *T* below T_{CO}, the $d_{Co2\text{-}O1/O2}$ expands while $d_{Co1\text{-}O1/O2}$ suddenly shrinks. Both distances approach constant values down to 5 K. The same behavior is shown by the mean Co-O distances ($\langle d_{Co\text{-}O}\rangle$) related to the Co2 and Co1 sites [Fig. 5(c)]. The evolution of $d_{Co\text{-}O}$ across T_{CO} provides evidence of a smaller volume of the Co1O$_5$ with respect to the Co2O$_5$ square pyramid. According to tabulated Shannon ionic radii,[18] this is consistent with Co1 and Co2 sites occupied by Co^{3+} and Co^{2+}, respectively.

To evaluate ionic charges of Co from the experimental $d_{Co\text{-}O,}$ we calculated BVS by using the tabulated parameters.[19] The results for all the cations of GBCO are shown in Fig. 6. BVS calculations for Gd and Ba cations gave reliable results yielding to valences of ≈2.9 and ≈2.1, respectively. No change in BVSs was observed above and below the CO transition, as shown in the inset of Fig. 6. Above T_{CO}, BVS related to Co provides evidence that the sites are occupied by cations in

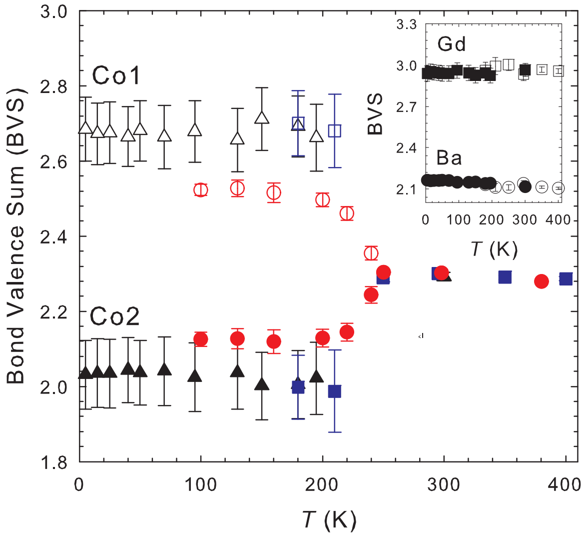

FIG. 6. (Color online) Temperature dependence of calculated BVS for Co in GBCO. Solid and open circles are data from SCD; solid and open squares and triangles are data from XRPD. In the inset the BVSs related to Gd and Ba are also shown.

mixed valence $+2.3$, a value slightly lower than that expected for a 1:1 ratio of Co^{2+}/Co^{3+}. Below T_{CO}, BVS found valences as large as ≈2.6 for the Co1 site and ≈2.0 for the Co2 site down to 5 K. According to Fauth *et al.*,[6] the *Pmma* structure can be described by an ordered alternation of $Co^{2+}O_5$ and $Co^{3+}O_5$ pyramids stacked along the *a* and *c* axes, while both $Co^{2+}O_5$ and $Co^{3+}O_5$ pyramids are allowed to run along the [010] direction (Fig. 1).

It should be noted that the estimated valence of the Co^{2+}/Co^{3+} in the *Pmmm* phase and Co1 sites in the *Pmma* phase sites are markedly lower than $+2.5$ and $+3$ expected values, respectively. Such deviations from formal reference values are rather common in perovskite compounds[20] and the observed valence depletion can be possibly due to a charge disorder affecting the Co sites. Moreover, this behavior is consistent with data reported for Ho and Tb parent compounds,[6] for which the calculated BVS suggest partial charge redistribution at both Co1 and Co2 sites.

B. PDF across the charge ordering transition

PDF analysis of the XRPD data collected at $T = 80$ K, 180 K, 298 K was carried out using the formalism of $G(r)$ functions. $G(r)$ is obtained via the sine Fourier Transform (FT) according to

$$G(r) = \frac{2}{\pi}\int_0^{Q_{\max}} Q[S(Q)-1]\sin(Qr)dQ, \qquad (1)$$

where $S(Q)$ is the total scattering structure function, $Q = 4\pi \sin\theta/\lambda$ and r is defined in the space of interatomic distances. $S(Q)$ is calculated from the experimental scattering intensity $I^{coh}(Q)$ containing both Bragg and diffuse scattering contributions. To consistently evaluate $I^{coh}(Q)$, the raw diffracted intensity profile $I(Q)$ collected at each temperature was corrected for background scattering, attenuation in the sample, and multiple and Compton scattering. The reduction process was done using the PDFGETX2 software[21] and full-structure profile refinements were carried out on the observed $G(r)$ using the PDFGUI program.[22] The program assesses the degree of accuracy of the refinement by the agreement factor R_w defined as

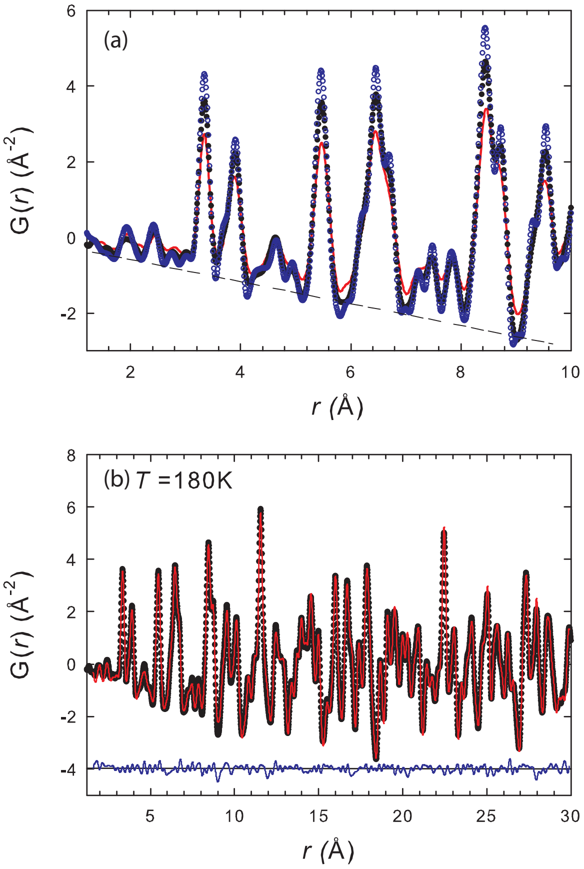

FIG. 7. (Color online) (a) PDFs obtained from GBCO sample at $T = 298$ K (continuous line), $T = 180$ K (solid circles), $T = 80$ K (open circles) within $r = 10$ Å. The dashed line is the baseline and corresponds to $-4\pi r\rho_0$. (b) Observed (dots) and calculated (continuous line) PDF obtained at 180 K within $r = 30$ Å. The residual plot is shown at the bottom of the figure.

$$R_W = \left[\frac{\sum w_i\left(G_i^{\exp} - G_i^{\text{calc}}\right)^2}{\sum w_i\left(G_i^{\exp}\right)^2}\right]^{1/2}, \qquad (2)$$

Figure 7(a) shows the experimental PDF curves obtained in the 1.3 Å $\leqslant r \leqslant$ 10 Å range. Each positive peak in $G(r)$ function is proportional to the probability of finding two atoms separated by a distance r averaged over all pairs of atoms in the sample. The main temperature-induced fluctuations in G(r) curves are given by the peak sharpening observed upon cooling. This is consistent with Debye law and therefore it cannot be considered as a response of the PDF to CO transition.

The experimental profiles were fitted in the 1.8 $\leqslant r \leqslant$ 30 Å range using the same structural models employed for interpreting the SCD and XRPD patterns. In general, they gave a good description of the PDF in a wide range of r, as testified by the good R_w values obtained: 0.082 ($T = 80$ K), 0.083 ($T = 180$ K), and 0.079 ($T = 298$ K). Focusing on the very short r range (1.8 $\leqslant r \leqslant$ 2.6 Å), Gd-O distances (at ≈2.4 Å) have weak T dependence, in agreement with the reciprocal

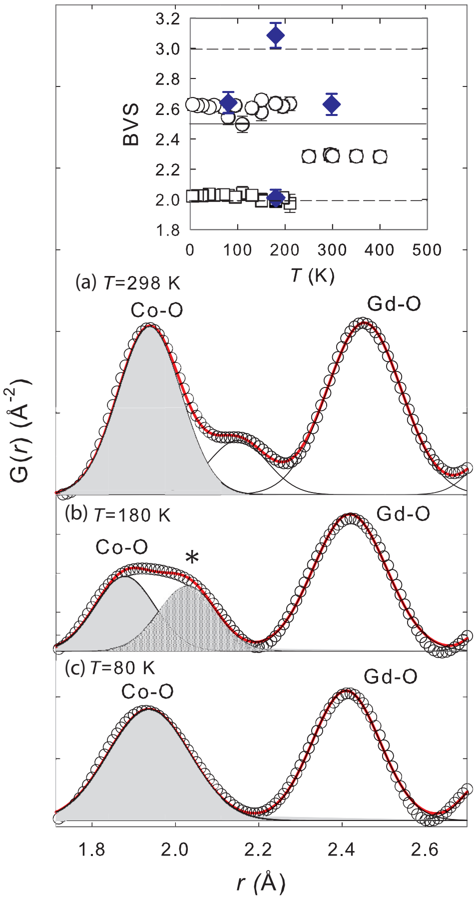

FIG. 8. (Color online) PDFs at short range. Open circles are the experimental curves and continuous lines are the fits showing the Co-O and Gd-O components of the PDF peaks. The "*" marked feature indicates the appearance of a bimodal Co-O bond length distribution (see text). The inset shows the local (diamods) and long-range (open circles and squares) bond valence sums (BVS) for Co as a function of T. Straight lines mark the expected BVS values for random and fully ordered Co^{2+}/Co^{3+} charge distributions (see text).

space analysis (see Fig. S1 in the Supplemental Material[13]). On the other hand, the short-range Co-O next-neighbor distances (in the $1.9 \leqslant r \leqslant 2.1$ Å range) show interesting features as a function of T. At 298 K PDF displays just a single peak near 2 Å besides the termination ripple at $r \approx 2.15$ Å [Fig. 8(a)]. At 180 K a bimodal distribution of the same PDF peak is found in agreement with the CO *Pmma* structure [Fig. 8(b)]. Indeed, below T_{CO} the originally single Co-O PDF peak splits into different bond length distributions [see Fig. 5 and the marked peak in Fig. 8(b)]. The integrated area ratio of these two new peaks is ≈1, suggesting a similar multiplicity of the atom pair *correlation*, consistent with different Co^{3+}/Co^{2+} oxygen bond distances. PDF analysis confirms that two distinct sites for Co^{3+} and Co^{2+} ions should be present at $T = 180$ K. Conversely, discrepancies between average and local structure are found at 80 K. The Rietveld analysis clearly indicates that the structure keeps two independent Co sites at this temperature but the experimental PDF at $T = 80$ K [Fig. 8(c)] exhibits a single-modal Co-O distance distribution. Moreover, the width of this peak is clearly increased in respect to higher T PDFs and is comparable with the overall width of the corresponding double peak at 180 K. This implies that the local average charge distribution of Co^{2+}/Co^{3+} ions differs from the long-range and that some kind of disorder should be present.

In order to get more quantitative information about the point charge distribution we estimated the *local* BVS and compared it with the *long*-range BVS obtained from the mean ⟨Co-O⟩ distances reported in Fig. 5(c). In these calculations, we constrained the Co-O distances in the pyramid to be the same. The inset of Fig. 8 shows the local average BVS together with expected Co charges for a full disordered (solid line) and full ordered (dashed line) phases. First, local BVS at $T = 298$ K is in very good agreement with a complete random occupation of Co^{2+} and Co^{3+} in a 1:1 ratio, whereas at $T = 180$ K it is consistent with a complete CO. On the other hand, at $T = 80$ K local BVS becomes very similar to the long-range BVS above T_{CO}. However, the increased width of Co-O peak suggests the contribution of several locally different Co-O distances due to a partial melting of charge localization at this temperature. This can be explained in terms of a weaker localization of the charge carriers, resulting in a smaller charge separation among symmetry-independent Co sites or, equivalently, in a reduction of the CO degree between Co atoms in the real space.

Accordingly, the intensity of the superstructure (102) reflection, which is greater than zero just in the *Pmma* phase, rapidly increases below ≈250 K, reaching a maximum at $T \approx 100$ K [Fig. 2(b)]. Below this temperature, its intensity begins to slightly decrease. At $T \approx 5$ K it roughly shows the same value as that measured at ≈200 K, which is ≈60% of its maximum value. The observed weakening of the (102) intensity is then consistent with a reduction of the CO state strength and agrees with the PDF outcome at $T = 80$ K.

C. EPR across the charge ordering transition

Figure 9 shows the EPR spectra as a function of temperature for GBCO sample. As found in $GdBaCo_2O_{5+\delta}$ compounds with $\delta \geqslant 0.5$, the signal consists of a single broad resonance line originating from the shift and/or broadening of the Gd^{3+} resonance, which in turn is caused by exchange interaction between localized $4f$ electron spin and the spins of Co atoms.[9] Looking at the temperature dependence of the EPR spectra, it

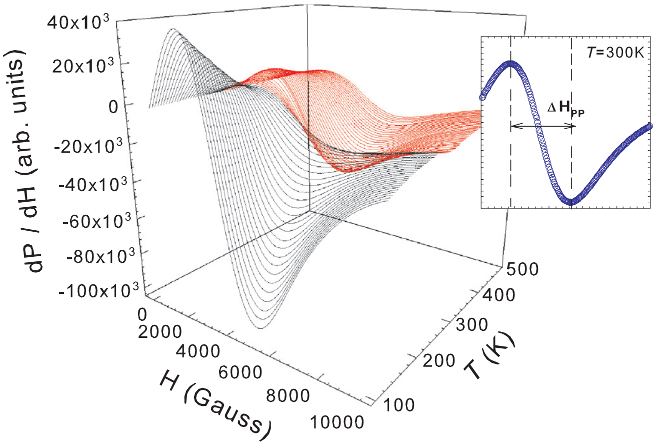

FIG. 9. (Color online) EPR spectra of the GBCO sample as a function of temperature. In the inset an example of observed EPR is shown.

is clear that the signals markedly change across the structural transitions. In principle, Lorentzian or Gaussian functions can be used to fit the spectra obtained from our powdered sample. However, attempts made by using the functions and linear combinations of these gave no improvement to the line-shape description. In this context, the analytical form of the Dysonian function gave better results and provides a description of the spectra at each T according to equation[23]

$$\frac{dP}{dH} \propto \frac{d}{dH}\left[\frac{\Delta H + \alpha(H - H_0)}{(H - H_0)^2 + \Delta H^2} + \frac{\Delta H + \alpha(H + H_0)}{(H + H_0)^2 + \Delta H^2}\right], \tag{3}$$

where ΔH is the linewidth, α is dispersion-to-absorption ratio, and H_0 is the resonance field.

However, Eq. (3) gives *only* a qualitative fit of the spectra. In particular, by comparing our spectra with Dysonian line reported in the literature for other perovskitic system,[23] we found our EPR measured spectra correspond only to a part of the literature reported line.[23] In particular, the left lobe of EPR spectrum shown in the inset of Fig. 9 is too broad to be fully observable. This could lead to unreliable numerical values of the (reciprocally correlated) ΔH, α, and H_0 parameters. For this reason, we decided to extract the peak-to-peak linewidth (ΔH_{pp}) as a direct observation of EPR data as depicted in the inset of Fig. 9.

The temperature dependence of ΔH_{pp} is shown in Fig. 10. In high-T PM regime regime (370 K $\leqslant T \leqslant$ 450 K), ΔH_{pp} decreases linearly by following the Korringa-type relation[24] $\Delta H_{\mathrm{pp}} = \Delta H^0_{\mathrm{pp}} + bT$ with $\Delta H^0_{\mathrm{pp}} = 2858(8)$ G and $b = 2.27(2)$ G/K. By further cooling, ΔH_{pp} shows a departure from the linear narrowing. On approaching T_{CO} upon cooling, ΔH_{pp} shows a weak drop at $T \approx 365$ K and it goes through a minimum at $T_{\mathrm{min}} \approx 300$ K. Below T_{min} the ΔH_{pp} has a complex thermal behavior. It displays a fast broadening, reaching a maximum value at $T \approx T_{\mathrm{CO}}$, and then rapidly decreases below T_{CO}. Interestingly, below 160 K the ΔH_{pp} seems to follow the linear temperature dependence observed at high T in the PM phase.

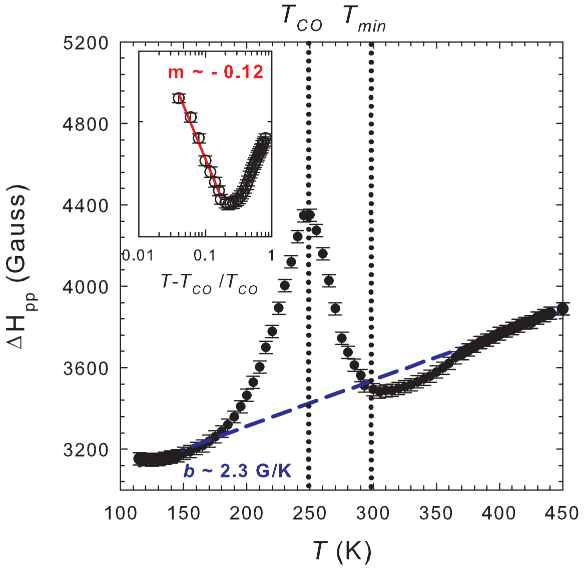

FIG. 10. (Color online) Temperature evolution of ΔH_{pp} for GBCO. The inset shows the log-log of the ΔH_{pp} as a function of $(T - T_{\mathrm{CO}}/T_{\mathrm{CO}})$.

IV. DISCUSSION

GBCO undergoes two structural phase transitions upon cooling. In our previous investigation[8] we found the first crystallographic transformation associated with a second-order phase transition. In particular, at $T \approx 350$ K the symmetry lowers from tetragonal ($P4/mmm$) to orthorhombic ($Pmmm$), inducing the loss of the C_4 axis along **c**. The breaking of the tetragonal symmetry perturbs the coordination environment around Gd and Co, and one half of oxygen atoms on the CoO$_2$ plane become symmetry independent below $T \approx 350$ K.

Below $T_{\mathrm{CO}} = 247$ K, a second structural phase transition takes place associated with the CO of the Co^{2+}/Co^{3+} ions. The space group changes from $Pmmm$ to $Pmma$, with the simultaneous doubling of the a axis. The analysis of the temperature dependence of the intensity of the $Pmma$ (116) superstructure reflection across this transition showed a critical exponent close to the ideal value for a second-order transition. However, Fauth *et al.*[6] studied the CO structural phase transition in the Tb, Dy, and Ho parent compounds[6] and some differences have to be noted. First, the transition temperature is significantly higher for the GdBaCo$_2$O$_5$ system ($T_{\mathrm{CO}} = 247$ K vs $T_{\mathrm{CO}} = 205$ K–215 K), suggesting that T_{CO} increases with the size of the rare-earth ion. It should be noted that such an increase is at least three times higher on passing from Tb to Gd (≈30 K) than on passing from Ho to Tb (≈10 K). Second, Fauth *et al.*[6] interpreted the CO phase transition as first order on the basis of their DSC measurements on the HoBaCo$_2$O$_5$ sample. All of this evidence suggests that the effect of Gd^{3+} on the transport and magnetic properties of the GBCO structure is critical and it implies a significant increase of the range of existence of the low-T CO $Pmma$ phase.

By further cooling, we found the signatures of a new structural anomaly. The depletion of the $Pmma$ (102) superstructure reflection below $T \approx 100$ K indicates that the CO state emerges at T_{CO} but weakens below ≈100 K. Accordingly, at $T = 80$ K the outcomes of our PDF analysis suggest that GBCO seems to recover a charge-disordered phase at the local scale. Due to the large width of the peak, the distance distribution of the Co-O first coordination shell is still consistent with the $Pmma$ structural model. However, the corresponding local BVS value suggests a partial melting of the charge localization. This structural difference between the local and the long-range scales is well known to occur in many strongly correlated perovskite like oxides showing properties such as magnetodieletric[25] or superconductivity.[26]

Reentrant CO behavior has been reported on LaSr$_2$Mn$_2$O$_7$ layered perovskite and its origin has been linked to the occurrence of a ferromagnetic-metallic state upon cooling.[2] As for the present case, possible reasons of this behavior can be investigated by considering the temperature evolution of spin relaxation as probed by EPR. Different relaxation mechanisms are known to result in a linear temperature dependence of ΔH_{pp} above the CO transition.[24] The decreasing ΔH_{pp} on cooling can be mediated by the exchange scattering between the local moments ($4f$ Gd^{3+} localized states) and itinerant charge carriers of Co ions. In the absence of bottleneck and dynamic effects, the b in Korringa-type relation is given by[24]

$$b = \frac{\pi k_B}{g\mu_B} N(E_F)^2 J^2, \tag{4}$$

where the term J_{fs} is the exchange coupling constant between the conduction electrons and localized spin and $N(E_F)$ stands for the density states at the Fermi energy.

The Korringa-type relaxation mechanism is governed by the scattering of conduction electrons off the EPR active spins, giving rise to linear temperature dependence of ΔH_{pp}.[24,27] In GBCO this could be consistent with the fairly low resistivity reported for $\text{GdBaCo}_2\text{O}_{5+\delta}$ ($\delta \to 0$) systems ($\approx$0.01 Ω cm at $T = 370$ K[7]), which implies a non-negligible delocalization for conduction electron in GBCO.[7] To account for the Korringa-type behavior in the charge-disordered PM phase, we consider that the electron delocalization of conduction electrons can be due to the motion of an extra electron from e_g level of Co^{2+} ion in high-spin (HS) configurations to an empty e_g orbital of Co^{3+} ion in intermediate-spin (IS) state. Note that these simple models imply double-exchange (DE) interactions between Co ions in different spin states, and they have been widely used to explain the insulator-to-metal transition observed in $\text{GdBaCo}_2\text{O}_{5+\delta}$ with $\delta \approx 0.5$.[9] The charge-disordered GBCO phase is characterized by a random distribution of $\text{Co}^{2+}/\text{Co}^{3+}$ and e_g electron hopping from an HSCo^{2+} to next ISCo^{3+} can give rise to electron delocalization in all the spatial directions. These isotropic DE paths between two pyramidal sites, defined as A and B can be sketched as

$$\begin{aligned} t_{2g}^5 e_g^2 - \text{HSCo}_\text{A}^{2+} + t_{2g}^5 e_g^1 - \text{ISCo}_\text{B}^{3+} &\to t_{2g}^5 e_g^1 - \text{ISCo}_\text{A}^{3+} \\ &+ t_{2g}^5 e_g^2 - \text{HSCo}_\text{B}^{2+}, \end{aligned} \tag{5}$$

It is worth noting that these exchange channels are reminiscent of the well-known DE between Mn^{3+} and Mn^{4+} invoked to correlate magnetic and electronic properties in mixed valence CO manganites.[1]

The temperature dependence of magnetization of YBaCo_2O_5 shows two anomalies at $T = 350$ K and $T_{\text{CO}} = 220$ K.[5,7] On the other side, PM contribution of Gd^{3+} dominates the magnetization of GBCO and no evidence of the existence of AFM transition has been reported in this system to date. Our ΔH_{pp} data observed on GBCO show a weak upturn at $T \approx 365$ K, which possibly mimics the drop observed on YBaCo_2O_5 at high temperature.[5,7] Moreover, $T \approx 365$ K perfectly matches with the onset of the tetragonal (200) peak broadening precursor of the $P4/mmm$ to $Pmmm$ transition.[8] This provides clear evidence which links the spin and lattice relaxation behaviors in GBCO.[8]

Basically, the emergence of AFM can be discussed by assuming that the structural transition is accompanied by a crossover from DE to superexchange Co-O-Co interactions. According to GK rules[6] the relevant superexchange couplings which hold for the AFM interactions in the $Pmmm$ phase are between HS-Co^{2+}-ISCo^{3+} along the [001] direction and HSCo^{2+}-HSCo^{2+}, IS-Co^{3+}-ISCo^{3+} along the [010] direction.[6] However, these magnetic interactions can be considered dominant only if a preliminary $\text{Co}^{3+}/\text{Co}^{2+}$ ordering is assumed at 365 K. Actually, incomplete or short-range CO has been invoked to explain the resistivity measurements in the $T_{\text{CO}} \leqslant T \leqslant 350$ K range of $Ln\text{BaCo}_2\text{O}_5$ parent compound.[6] However, we did not observe any signature of the CO phase in the short-range PDF of GBCO at RT.

AFM interactions between Co ions and partial conduction electron delocalization can generate short-range AFM correlation between Gd^{3+} through the Ruderman-Kittel-Kasuya-Yosida (RKKY) interaction. In the 247 K $\leqslant T \leqslant$ 365 K range, the conduction electrons are mobile to some extent and they can transfer the Co AFM spin fluctuations to the Gd sites *via* the RKKY mechanism. This gives rise to an effective alternating internal magnetic field which relaxes the Gd spins. In principle, upon cooling one could expect an increase of the spin relaxation rate of Gd^{3+}, which produces the broadening of the EPR signal. This is exactly what is observed in our EPR data below $T_{\text{min}} \approx 300$ K (see Fig. 10). The EPR line broadening while decreasing T has been interpreted as a precursor behavior of AFM transitions.[28,29] According to available theories,[28] the critical increase of ΔH_{pp} due to AFM spin fluctuations can be described by the relation $\Delta H_{\text{pp}} = a[(T - T_\text{C})/T_\text{C}]^{-m}$, where a, m are constants and T_C is the critical temperature, i.e., $T_\text{C} = T_{\text{CO}}$ in the present case. In our data, ΔH_{pp} starts to increase at $T_{\text{min}} \approx 1.2T_{\text{CO}}$ and rapidly broadens as T_{CO} is approached from above. In the inset of Fig. 10 the log-log plot of ΔH_{pp} as a function of $[(T - T_{\text{CO}})/T_{\text{CO}}]$ is shown. A linear correlation is evident just above T_{CO}, analogous to that expected near Néel temperature for AFM spin fluctuations.[28] We determined $m = -0.12$ in agreement with that found in other layered compounds where the Gd^{3+} spin dynamics is affected by $3d$ metal spins fluctuations.[28,29]

Spin fluctuations above T_{CO} as revealed by EPR can be then considered precursors of magnetic transition at T_{CO}.[28] This gives a new insight to reappoint the actual T_N in $Ln\text{BaCo}_2\text{O}_5$ system. Indeed, we propose that the weak upturn at 365 K is more related to the onset of short-range CO giving rise to AFM spin fluctuations between the partially ordered Co. When T is further lowered, according to GK rules, the long-range CO drives the AFM ordering which destroys the spin fluctuations at T_{CO}. In this context, $T \approx 250$ K $\approx T_{\text{CO}}$ should be set as the actual Néel temperature. This is consistent with the magnetization of YBaCo_2O_5 which shows a more marked drop at $T_{\text{CO}} = 220$ K than at 350 K.[5,7]

The emergence of long-range CO is therefore associated with a strong localization of the conduction electrons that weakens the RKKY coupling between Co and Gd below T_{CO}. Since the superexchange interactions are stronger and not frustrated within the 3D CO network,[6] the overall AFM coupling increases with CO distortion. Because of the AFM ordering, the internal field owing to spin fluctuations disappears and the EPR signal is dominated by the PM contribution of Gd^{3+} spins, which narrows ΔH_{pp} on cooling. Below 160 K, ΔH_{pp} seems to follow the same linear temperature dependence observed at high T. Looking at our data in the low-T region, the temperature dependence of ΔH_{pp} is indeed similar to that observed in the PM phase. Reentrant PM behavior has been also observed at $T = 75$ K in $\text{GdBaCo}_2\text{O}_{5.5}$ and the transition has been associated to a spin-state transition (SST) from IS to a low-spin (LS) $t_{2g}^6 e_g^0$ state at Co^{3+} site.[30] SST involving the same Co^{3+} spin states was also reported for LaCoO_3 at $T \approx 100$ K.[31] Moreover, the switch from IS to LS of Co^{3+}

introduces nonmagnetic ions within the superexchange framework of the CO phase of GBCO. As a result, superexchange couplings involving Co^{3+} disappear, disrupting the AFM order that gradually weakens on cooling. Since in the CO phase the electron localization is mainly driven by AFM couplings between ordered Co^{2+}/Co^{3+}, the emergence of PM phase at low T well matches the partial melting of charges localization observed from structural analysis.

To explain the interplay between the structural and magnetic ground-state evolution as a function of T in GBCO we propose the following mechanism. According to DE between the randomly distributed $HSCo^{2+}$ and $ISCo^{3+}$, the conduction electrons in the high-T PM phase are delocalized to some extent. On going through $T \approx 365$ K, the Co^{2+}/Co^{3+} ions start to partially order, leading to the coexistence of both localized and delocalized charge carriers. Because of incomplete CO, the crossover from DE to superexchange interactions gives rise to RKKY couplings between short-range AFM and Gd^{3+} spins. At $T_{\rm min} \approx 1.2 T_{\rm CO}$ the emergence of AFM spin fluctuations are a precursor effect of the AFM transition associated with the onset of CO. Once the long-range CO is initiated the density of delocalized conduction electrons rapidly decreases. As a result, $\Delta H_{\rm pp}$ decreases on cooling and below $T \approx 160$ K it gradually approaches the linear T dependence observed in the high-T PM phase. Below this point, we observed the mismatch between the local and the average BVS and the decrease of superstructure reflection intensity, suggesting a reentrant behavior of CO. These latter observations, together with $T_{\rm N} \approx T_{\rm CO}$, lead us to believe that CO layered cobaltite shows strong similarity with manganites.[1–4]

V. CONCLUSION

In the present study we have clearly revealed the intimate interplay of electron localization and magnetic spin ordering in GBCO. The second-order *Pmmm* to *Pmma* structural phase transition associated with CO at $T_{\rm CO} = 247$ K was directly observed by SCD and XRPD techniques. In particular, the emerging of the CO phase is supported by (i) the behavior of the superstructure reflections, (ii) the temperature dependence of the Co-O distances, and (iii) the computed BVS. EPR measurements gave important insights into the CO transition holding the emergence of spin fluctuations at $T_{\rm min} \approx 1.2\ T_{\rm CO.}$ As reported for other layered compounds,[28,29] the spin fluctuations can be considered a precursor effect of AFM transition associated to the onset of long-range CO in GBCO system. Hence, in agreement with the $YBaCo_2O_5$ magnetization curve, which shows a more marked drop at $T_{\rm CO} = 220$ K than at 350 K,[5,7] we suggest that the long-range AFM order takes place at $\approx T_{\rm CO}$ in GBCO.

PDF analysis of diffraction data shows new structural features. At 298 K and 180 K the local structure is consistent with a fully random occupation of Co^{2+} and Co^{3+} in a 1:1 ratio and with a complete CO. On the other hand, at $T = 80$ K the local-range PDF seems to be consistent with a melting of charges localization. In turn, this suggests that a reentrant CO transition occurs in GBCO. This behavior, analogous to that found in CMR manganites,[2] is supported by the temperature dependence of $\Delta H_{\rm pp}$ below 160 K and is consistent with the PM reentrant behavior found for the $GdBaCo_2O_{5.5}$ parent compound.

ACKNOWLEDGMENTS

The authors gratefully acknowledge the European Synchrotron Radiation Facility for provision of beam time and Dr. Adrian Hill for assistance in using the ID31 beamline. The authors would like to thank Dr. D. Chernyshov for useful discussions. The Danish National Research Foundation through the Center for Materials Crystallography (CMC) has also been very much appreciated.

---

[*] mattia.allieta@gmail.com

[1] J. P. Joshi, R. Gupta, A. K. Sood, S. V. Bhat, A. R. Raju, and C. N. R. Rao, Phys. Rev. B **65**, 024410 (2001), and references therein.

[2] T. Chatterji, G. J. McIntyre, W. Caliebe, R. Suryanarayanan, G. Dhalenne, and A. Reveolevschi, Phys. Rev. B **61**, 570 (2000).

[3] J. C. Loudon, N. D. Mathur, and P. A. Midgley, Nature (London) **420**, 797 (2002).

[4] A. A. Taskin and Y. Ando, Phys. Rev. Lett. **98**, 207201 (2007).

[5] T. Vogt, P. M. Woodward, P. Karen, B. A. Hunter, P. Henning, and A. R. Moodenbaugh, Phys. Rev. Lett. **84**, 2969 (2000).

[6] F. Fauth, E. Suard, V. Caignaert, B. Domengès, I. Mirabeau, and L. Keller, Eur. Phys. J. B **21**, 163 (2001).

[7] A. A. Taskin, A. N. Lavrov, and Y. Ando, Phys. Rev. B **71**, 134414 (2005).

[8] L. Lo Presti, M. Allieta, M. Scavini, P. Ghigna, L. Loconte, V. Scagnoli, and M. Brunelli, Phys. Rev. B **84**, 104107 (2011).

[9] M. Allieta, C. Oliva, M. Scavini, S. Cappelli, E. Pomjakushina, and V. Scagnoli, Phys. Rev. B **84**, 235144 (2011), and references therein.

[10] X. F. Sun, A. A. Taskin, X. Zhao, A. N. Lavrov, and Y. Ando, Phys. Rev. B **77**, 054436 (2008).

[11] X. S. Wu, H. L. Zhang, J. R. Su, C. S. Chen, and W. Liu, Phys. Rev. B **76**, 094106 (2007).

[12] *CrysAlisPro RED Software System*, Ver. 1.171.33.32 (Oxford-diffraction Ltd., Oxford, England, 2009).

[13] See Supplemental Material at http://link.aps.org/supplemental/10.1103/PhysRevB.88.214104 for assessment of the sample quality and tables containing refined structural parameters obtained from the synchrotron SCD and XRPD data collected at selected temperatures.

[14] G. M. Sheldriek, SHELXL97 (University of Göttingen, Göttingen, Germany, 1997).

[15] A. C. Larson and R. B. Von Dreele, General Structure Analysis System (GSAS), Los Alamos National Laboratory Report LAUR 86-748 (2004).

[16] G. M. Sheldrick, Acta Crystallogr. A **64**, 112 (2008).

[17] D. Chernyshov, V. Dmitriev, E. Pomjakushina, K. Conder, M. Stingaciu, V. Pomjakushin, A. Podlesnyak, A. A. Taskin, and Y. Ando, Phys. Rev. B **78**, 024105 (2008).

[18] R. D. Shannon, Acta Crystallogr. A **32**, 751 (1976).

[19] http://www.iucr.org/resources/data/datasets/bond-valence-parameters.

[20] S. Streule, M. Medarde, A. Podlesnyak, E. Pomjkushina, K. Conder, S. Kazakov, J. Karpinski, and J. Mesot, Phys. Rev. B **73**, 024423 (2006).

[21] X. Qiu, J. W. Thompson, and S. J. L. Billinge, J. Appl. Crystallogr. **37**, 678 (2004).

[22] C. L. Farrow, P. Juhás, J. W. Liu, D. Bryndin, E. S. Božin, J. Bloch, Th. Proffen, and S. J. L. Billinge, J. Phys.: Condens. Matter **19**, 335219 (2007).

[23] J. P. Joshi and S. V. Bhat, J. Magn. Reson. **168**, 284 (2004).

[24] C. Rettori, S. B. Oseroff, D. Rao, P. G. Pagliuso, G. E. Barberis, J. Sarrao, Z. Fisk, and M. Hundley, Phys. Rev. B **55**, 1016 (1997).

[25] M. Allieta, M. Scavini, L. J. Spalek, V. Scagnoli, H. C. Walker, C. Panagopoulos, S. S. Saxena, T. Katsufuji, and C. Mazzoli, Phys. Rev. B **85**, 184107 (2012).

[26] M. Scavini, M. Coduri, M. Allieta, L. Mollica, M. Brunelli, L. Malavasi, A. Lascialfari, and C. Ferrero, J. Phys. Chem. C **114**, 19509 (2010).

[27] S. Schaile, H.-A. Krug von Nidda, J. Deisenhofer, A. Loidl, T. Nakajima, and Y. Ueda, Phys. Rev. B **85**, 205121 (2012).

[28] Claudiu Filip, Liviu Giurgiu, Xenia Filip, Cristoph Kessler, and Michael Mehring, Czech. J. Phys. **46**, 1143 (1996).

[29] F. J. Owens, Physica C **353**, 265 (2001).

[30] W. S. Kim, E. O. Chi, H. S. Choi, N. H. Hur, S.-J. Oh, and H.-C. Ri, Solid State Commun. **116**, 609 (2000).

[31] K. Asai, A. Yoneda, O. Yokokura, J. M. Tranquada, G. Shirane, and K. Kohn, J. Phys. Soc. Jpn. **67**, 290 (1998).